



In vivo-driven optimization of finite element models' parameters for capturing altered mechanics in patients with Achilles tendinopathy

Alessia Funaro ^{a,*} , Vickie Shim ^b, Ine Myns ^a, Chun Vong ^b, Benedict Vanwanseele ^a

^a Human Movement Biomechanics Research Group, Department of Movement Science, KU Leuven, Belgium

^b Auckland Bioengineering Institute, University of Auckland, Auckland, New Zealand

ARTICLE INFO

Keywords:

Achilles tendon
Subtendon sliding
Material properties
Finite element models
Optimization routine
Rehabilitation

ABSTRACT

Patients with Achilles tendinopathy exhibit altered tendon mechanics, including changes in the sliding behaviour of Achilles tendon (AT) subtendons and variations in material properties. These individual mechanical alterations influence the AT's response to load and the resulting strains, which are critical for understanding the mechanisms underlying Achilles tendinopathy and promoting effective recovery. The goal of this study was to develop an optimization routine to determine 1) patient-specific AT mechanics, representing the altered sliding mechanisms and 2) patient-specific material properties of the AT, thereby offering a more individualized depiction of the tendon's response under load. Thirteen patients with Achilles tendinopathy were imaged at rest using three-dimensional freehand ultrasound. The images were manually segmented to create finite element models with patient-specific AT shapes, which also incorporated the twisted geometry of the subtendons. The optimization routine was informed by various *in vivo* experimental data, including AT elongations estimated during sub-maximal voluntary isometric contraction (measured via three-dimensional freehand ultrasound) for material coefficient estimation, as well as localized AT differential displacement (measured via ultrasound speckle tracking) for friction coefficient estimation. Additionally, patient-specific maximal voluntary isometric contraction (MVIC) force estimations were integrated into the model. This optimization process identified patient-specific material and friction coefficients for the finite element models, enabling the closest possible alignment with experimental observations. By incorporating altered tendon properties, such as subtendon sliding and material characteristics, the routine provides a tool for future applications which aim to gain a comprehensive understanding of the individualized AT response to load and offer valuable insights for managing Achilles tendinopathy.

1. Introduction

The complexity of tendinopathy's mechanisms is influenced by multiple factors, including tendon mechanics, such as the intratendinous sliding, and material properties, both of which are altered in affected individuals (Arya and Kulig, 2010; Couppé et al., 2020). The AT is composed of three subtendons from the triceps surae muscles (soleus (SOL), gastrocnemius medialis (GM), and lateralis (GL)), which exhibit a unique twisted structure (Pekala et al., 2017), allowing relative motion between fascicle bundles (Franz et al., 2015). Indeed, an ultrasound speckle tracking study (Bogaerts et al., 2017) observed non-uniform displacement and regional strain within the AT. One of the primary contributors to this non-uniform displacement was identified as intratendon sliding (Handsfield et al., 2017). The relative sliding of fascicles

is believed to facilitate a more uniform distribution of forces, thereby minimizing the risk of localized overstrain that could lead to injury or degeneration. Similarly, subtendon sliding has been proposed, as subtendons are thought to slide relative to one another (Handsfield et al., 2020). However, a compromised sliding mechanism is evident in patients with Achilles tendinopathy, with reduced intratendinous sliding observed during muscle contraction (Lecompte et al., 2024). Some evidence suggested that collagen proliferation, scar tissue formation or alterations in lubricin concentration could explain lower sliding in Achilles tendinopathy (Arnoczky, Lavagnino and Egerbacher, 2007; Magnusson, Langberg and Kjaer, 2010; Thorpe and Screen, 2016). In addition, it has been demonstrated that the tensile modulus decreases in patients with Achilles tendinopathy compared to healthy individuals (Arya and Kulig, 2010). Therefore, it is crucial to consider both the

* Corresponding author at: Tervuursevest 101 box 1501, 3000 Leuven, Belgium.

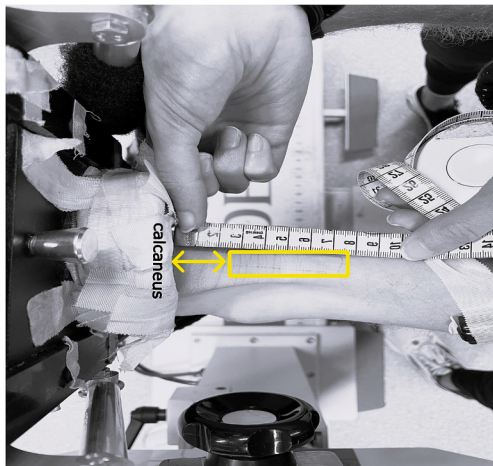
E-mail address: alessia.funaro@kuleuven.be (A. Funaro).

altered sliding mechanisms and material properties, especially when evaluating tendon strains. Both sliding mechanism and material properties significantly influence strain behaviour (Handsfield et al., 2017; Hansen et al., 2017), which play a key role in the recovery process from Achilles tendinopathy (Arampatzis et al., 2007; Wang et al., 2015). Additionally, patient-specific estimation of these characteristics would allow the consideration of interindividual differences. This approach is essential for a more comprehensive understanding of the mechanisms underlying Achilles tendinopathy.

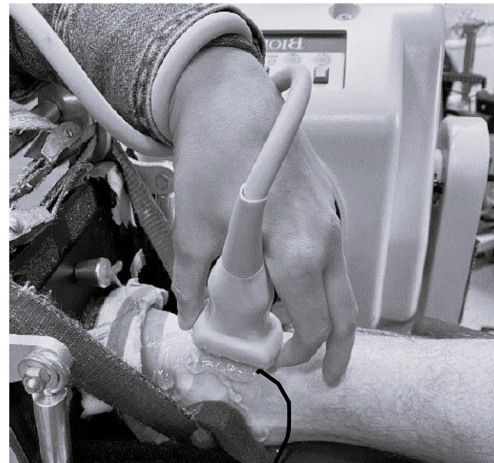
Finite element (FE) models are a valuable tool for understanding internal tendon strains, allowing for the incorporation of subject-specific features such as AT shape (Diniz et al., 2023; Funaro, 2022; Handsfield, 2020; Hansen, 2017; Shim, 2014), material properties (Hansen et al., 2017; Shim et al., 2019), and muscle forces (Funaro et al., 2022), as well as the complex geometry of twisted subtendons (Handsfield et al., 2017; Funaro et al., 2022). These models can also be used for estimating mechanical and material properties, which can be crucial in patients with Achilles tendinopathy, where such properties are altered. A common approach in FE modelling is to conduct an inverse FE analysis, where an optimization algorithm iteratively adjusts model parameters to closely match experimental observations, minimizing error (Hansen et al.,

2017; Shim et al., 2019). However, current FE models often fall short in representing Achilles tendinopathy, particularly due to a lack of patient-specific subtendon structure. Most are based on healthy individuals (Funaro et al., 2022), despite known structural changes in tendinopathy (Nuri et al., 2018) and individual variability (Funaro et al., 2025). Furthermore, many models omit subtendon architecture (Shim et al., 2014, 2019; Hansen et al., 2017), which is crucial for capturing the non-uniform sliding behaviour of the AT. However, previous models of healthy participants have typically represented subtendon contact as frictionless (Funaro et al., 2022), limiting their applicability to pathological conditions. Other studies (Diniz et al., 2023; Handsfield, 2017; Yin et al., 2021) explored different contact conditions in AT FE models from healthy individuals, using either frictionless sliding, tied interfaces, or generic friction coefficients. However, these conditions cannot capture the individual alterations in the sliding mechanism seen in tendinopathy. Regarding material properties, inverse FE modelling was employed to estimate these parameters in patients with Achilles tendinopathy. However, these coefficients are population-specific, and applying them to patient-specific AT strain estimations in a different cohort may result in inaccurate predictions. This is because material properties vary between individuals and influence AT strain behaviour

A) Distance of the tendinopathic area from calcaneus



B) Placement of the probe



C) Ultrasound speckle tracking

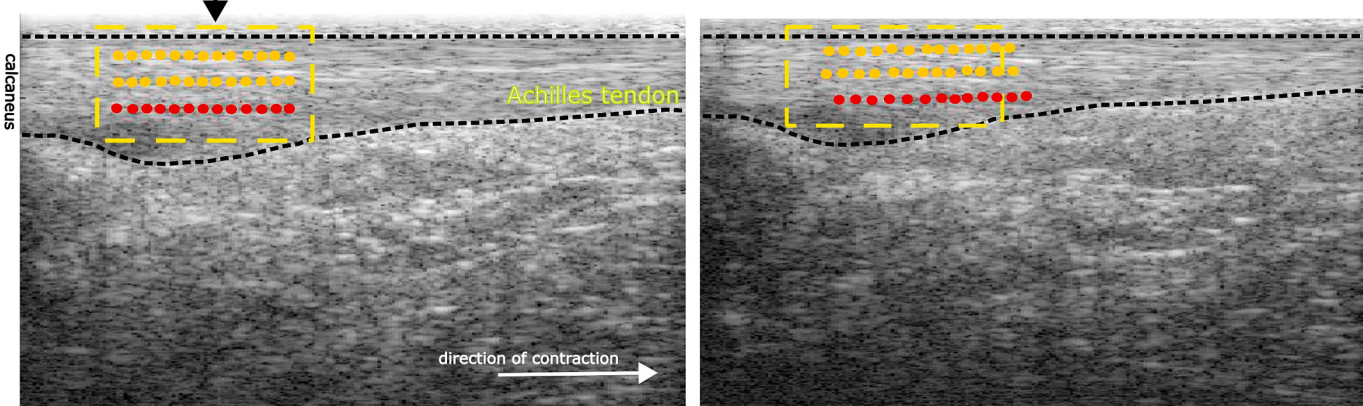


Fig. 1. The images show the experimental data collection process, followed by the analysis routine for ultrasound speckle tracking. During data collection, the probe was positioned over the tendinopathic region, and its location was measured using a measuring tape, with the calcaneus serving as the anatomical reference point (A). Once the correct position was determined, the probe was positioned to record the ultrasound speckle tracking data (B). In the 2D ultrasound image, the tendinopathic region was observable, and the region of interest (ROI), marked by a yellow box, was defined for tracking the displacement of the fascicles by considering three layers within the tendon. During 30% and 60% MVIC, the tendon layers move in the direction of contraction, and the speckles within the ROI follow their displacement (C).

(Hansen et al., 2017; Shim et al., 2019). There is a need for patient-specific FE models that represent the altered sliding mechanisms and material properties in patients with Achilles tendinopathy. Such models should integrate patient-specific MVIC forces and AT shape, and twisted subtendons geometry to provide a more comprehensive analysis and enable accurate patient-specific estimates of AT strains. Such an approach will contribute to a more tailored understanding of Achilles tendinopathy.

The objective of this study was to develop FE models of the AT that incorporated the *in vivo* measurements, such as patient-specific MVIC forces and AT shape, to simulate AT individual responses in patients with Achilles tendinopathy. To achieve that, this study introduced a two-step optimization routine designed to determine patient-specific material coefficients and friction coefficient between two subtendon layers of individuals with Achilles tendinopathy. Our hypotheses were twofold: 1) We can develop a workflow that optimizes both the material properties of the subtendons and the friction coefficient describing the resistance to sliding between two subtendon layers, and 2) The optimized material properties will be reasonable based on literature data.

2. Material and Methods

2.1. Participants characteristics

Thirteen participants with midportion Achilles tendinopathy (11 males, 2 females; age: 47 ± 14 years, height: 181 ± 7 cm, weight: 79 ± 15 kg) were included in the study, according to the inclusion and exclusion criteria formulated by Arya and Kulig (2010). All participants completed the Victorian Institute of Sport Assessment-Achilles questionnaire (VISA-A) (Craig et al., 2003), which provides an index of Achilles tendinopathy pain and functioning (VISA-A score: 70 ± 21). The study was approved by the local ethical committee UZ/KU Leuven (S63532).

2.2. Experimental data collection

The participants lay prone on an isokinetic dynamometer (Biodex system 4 MVP, Biodex Medical Systems, New York, USA). The knee was fully extended, and the ankle angle was positioned at a 90-degree angle, while being aligned with the axis of rotation. After a standardized warm up, each participant performed two repetitions of a 5-second maximum voluntary isometric contraction (MVIC). The highest value was then used to estimate the target sub-maximal torque for subsequent testing tasks.

Three-dimensional freehand ultrasound (3DfUS) images were acquired under resting conditions to estimate the free AT resting length and generate a patient-specific mesh. Additionally, six sustained contractions at 30% and 60% of maximal torque were performed in randomized order to subsequently calculate tendon elongation. Images were acquired at a 40 mm depth and a 30 Hz frame rate, covering the region from the distal calcaneus to the SOL myotendinous junction. The acquisition was performed using 3D Slicer software (slicer.org; v4.10.1; Perth, Australia) (Fedorov et al., 2012). The ultrasound machine was integrated with an optical motion tracking system (V120 tracking system, Optitrack, Corvallis, OR, USA) to generate a 3D reconstruction of the free AT. These measurements were used for the material coefficients optimization.

During three 5-second ramped contractions aiming to reach 60% of maximal torque, speckle tracking images of the AT were captured. Ultrasound speckle tracking acquisitions, which combine B-mode ultrasound and radiofrequency data (ArtUs RF-Data Control, v1.4.4), were collected at 70 frames per second using a conventional 2D ultrasound machine (ArtUS, UAB Telemed, Vilnius, Lithuania) with a 40-mm linear transducer (L15-7H40-A5, ArtUs EXT-1H system, UAB Telemed, Vilnius, Lithuania). The linear probe was placed over the tendinopathic area of the AT, characterized by significant focal thickening of the tendon. The

location of the probe was marked with a tape (Fig. 1), and the distance from the calcaneal notch to the tape was measured to determine the probe's positioning, which was then used in the friction coefficient optimization routine.

2.3. Estimation of *in vivo* input parameters for optimization routine

From the 3DfUS acquisitions, AT lengths at rest, 30% and 60% MVIC were measured as the distance between the most distal edge of the calcaneal notch and the SOL myotendinous junction. The AT elongations at 30% and 60% MVIC (MTJ_{exp}) were then calculated by subtracting the resting length from the lengths observed during the two sub-maximal sustained contractions.

Localized AT tissue displacements during the ramped contractions were examined using a validated ultrasound speckle tracking algorithm in Matlab 2020b (Chernak Slane and Thelen, 2014; Dandois et al., 2021). Parameters for data reduction and analysis, such as kernel size, search window sizes, and cross-correlation threshold, were determined based on prior research (Crouzier et al., 2022). Differential displacement (Δd_{exp}) within the AT was calculated as the difference between the bottom layer displacement and the average of the top and middle layers displacements. The bottom layer was assigned to the SOL subtendon and the upper and the mid layer to the GM and GL subtendons (Clark and Franz, 2018). This configuration corresponds to the subtendon twisting geometry later implemented in the AT models, as explained in the “*Generation of Patient-Specific FE Models*” section, and reflects the assumptions made for optimizing the friction coefficient, as outlined in the “*Estimation of the Material and Friction Coefficients*” section.

For the optimization routine, we estimated the forces of each of the three triceps surae muscles during 30% and 60% MVIC to serve as boundary conditions for the FE models. First, we calculated the total patient-specific force of the triceps surae muscles during 30% and 60% MVIC, from the patient-specific sub-maximal torques and moment arms (Merza et al., 2021). Then, the three triceps surae muscle forces were generically distributed as follows: 11% for the GL muscle, 27% for the GM muscle, and 62% for the SOL muscle (Albracht, Arampatzis and Baltzopoulos, 2008).

2.4. Generation of the patient-specific FE models

FE models with patient-specific AT shape were generated using the AT reconstructions recorded at rest. The free-form deformation method (Fernandez et al., 2018) was then applied to define the twisted subtendons geometry within this individualized shape (Funaro et al., 2025) (Fig. 2). This method adjusted all nodes in the FE model, resulting in subject-specific geometry for both outer and subtendon parts. A more detailed description of the FE model geometry, subtendon definition, and the morphing routine used can be found in our previous work (Funaro et al., 2025) and *Supplementary Materials*. The average root mean square (RMS) error between the patient-specific point cloud and the morphed mesh was 0.68 ± 0.03 mm. The subtendons model was meshed using 8-node hexahedral solid elements. The distal end of the tendon models was fixed to mimic the attachment of the tendon to the calcaneus. Muscle forces at 30% and 60% MVIC were applied as distributed nodal loads to the proximal faces of each corresponding subtendon. The nodal displacements were constrained to move only in the distal–proximal direction.

The constitutive model was defined as “*trans iso Mooney-Rivlin*” in FEBio Studio (Maas et al., 2012). The tendon was modelled as an incompressible, transversely isotropic hyperelastic material, following the formulation by Weiss et al. (1996). Three coefficients of the constitutive model, C_1 , C_4 , and C_5 , were optimized. Specifically, C_1 characterizes the isotropic ground substance matrix, while C_4 represents the rate of collagen fibre uncrimping, and C_5 corresponds to the Young's modulus of the straightened collagen fibres. Additional details about the constitutive model are provided in the *Supplementary Materials*.

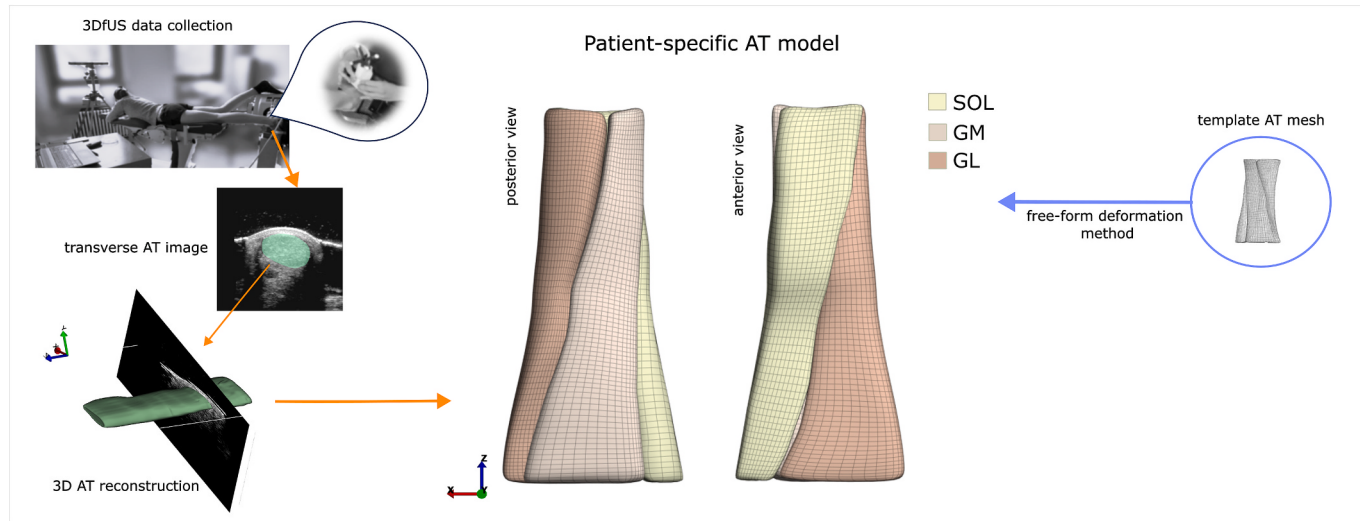


Fig. 2. The figure illustrates the experimental data collection and analysis steps to obtain the AT mesh, where the participant was lying prone on the Biodex table. Tendon images were collected at rest using 3DfUS, with the probe held with a custom-made holder equipped with markers. These markers, visible in the close-up image, were tracked by the Optitrack system, located at the top left of the figure. Consecutive transverse AT images were obtained from the calcaneus to the SOL myotendinous junction, enabling the reconstruction of a 3D model of the tendon, which serves as the patient-specific AT shape. The final AT model incorporated three subtendons, developed from a template and integrated into the patient-specific mesh using the free-form deformation method.

2.5. Estimation of the material and friction coefficients

The material and friction coefficients were determined via a two-step parameters optimization routine: 1) the AT elongations during 30% and 60% MVIC for material coefficients optimization, and 2) the Δd_{exp} obtained from speckle tracking data for friction coefficient optimization.

For the material coefficients optimization, the boundary conditions simulated the 30 % and 60 % MVIC condition (see Section 2.2). The displacement of the nodes of the entire SOL subtendon in the AT models was compared with the experimental AT elongations estimated from the 3DfUS images during 30% and 60% MVIC (Fig. 3). During this step, the contact was maintained as frictionless. Optuna optimization (Akiba et al., 2019) suggested values for the material coefficients that minimize the total error, $error_{mp}$. The $error_{mp}$ is the sum of the relative errors for the two conditions, 30 % and 60 % MVIC. The relative errors were defined as follows (1):

$$error\%_{MVIC} = \frac{(SOL_{sim} - MTJ_{exp})^2}{(MTJ_{exp})^2} \quad (1)$$

where the $error\%_{MVIC}$ is the relative error calculated for each of the two %MVIC levels (30% and 60%), SOL_{sim} is the simulated displacement of the SOL subtendon, MTJ_{exp} is the displacement of the SOL myotendinous junction observed in experiments. The total error $error_{mp}$ for the material coefficients optimization was then defined as follows (2):

$$error_{mp} = error_{30\%} + error_{60\%} \quad (2)$$

These optimized values were then used as material coefficients for the FE model in the friction coefficient optimization. During this step, a tied contact was applied between the GM and GL subtendons to fix them together, which will be referred to as GAS from now on. This approach was necessary because speckle tracking could not distinguish between GM and GL. It assumes that the friction coefficient between the SOL subtendon and the GM and GL subtendons is uniform. The contact between the SOL subtendon and GAS subtendons was defined as sliding elastic, while the friction coefficient between the subtendons was iteratively changed to match the experimental data. Between the contact surfaces, the augmented Lagrangian method was used for constraint enforcement (Zimmerman and Ateshian, 2018). A ROI within the FE was identified using a distance-based mapping approach, which accounted

for the probe's location on the tendon (see Section 2.2) to match the area where localized AT differential displacement Δd_{exp} was assessed (Fig. 3). Subsequently, the average displacements of the nodes within the ROI were calculated for the SOL and the GAS subtendon, referred to as *SOL displacement* and *GAS displacement*, respectively. The simulated differential displacement (Δd_{sim}) was then derived by subtracting *GAS displacement* from *SOL displacement*. Then, the relative error ($error_{fc}$) between the simulated, Δd_{sim} , and experimental differential displacement, Δd_{exp} , (see Section 2.3) was computed and used as the objective function of the Optuna optimization (3):

$$error_{fc} = \frac{(\Delta d_{sim} - \Delta d_{exp})^2}{\Delta d_{exp}^2} \quad (3)$$

Reduced subtendon sliding in Achilles tendinopathy (Lecompte et al., 2024) is linked to changes in tendon composition, though the exact physiological mechanisms are still unknown. In our model, this was represented as contact with friction. Future research is needed to explore the underlying biological changes contributing to this reduced sliding.

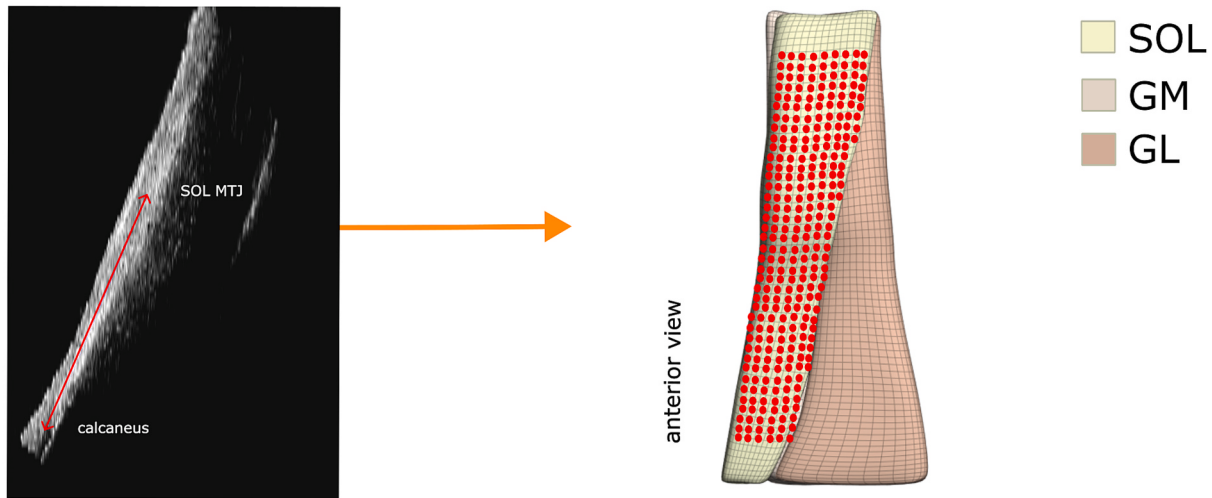
2.6. Sensitivity analysis

Since our material and friction coefficient optimization were done on two distinct datasets, we performed two separate sensitivity analyses to see the sensitivity of optimised parameters: 1) a Sobol sensitivity analysis for the material coefficients and 2) a one-way sensitivity analysis for the friction coefficient.

Sobol's variance-based sensitivity analysis decomposed the variance of the model output into contributions from individual input parameters (three material parameters, C_1 , C_4 , and C_5) and their interactions (Sobol, 2001). The output was the objective function of the optimization for the material parameters $error\%_{MVIC}$ (for details, see Section 2.5, equation (2)). The Sobol indices were computed using Python's SciPy package (Virtanen et al., 2020).

The one-way sensitivity analysis involved varying the friction coefficient while holding all other factors constant, to observe the impact of variations in the friction coefficient on the output $error_{fc}$ (see Section 2.5, equation (4)), which is the objective function for optimizing the friction coefficient. The friction coefficient, defined between 0 and 1, was adjusted in increments of 0.01, and the corresponding value of the $error_{fc}$

A) AT elongation from 3DfUS



B) Differential displacement from ultrasound speckle tracking

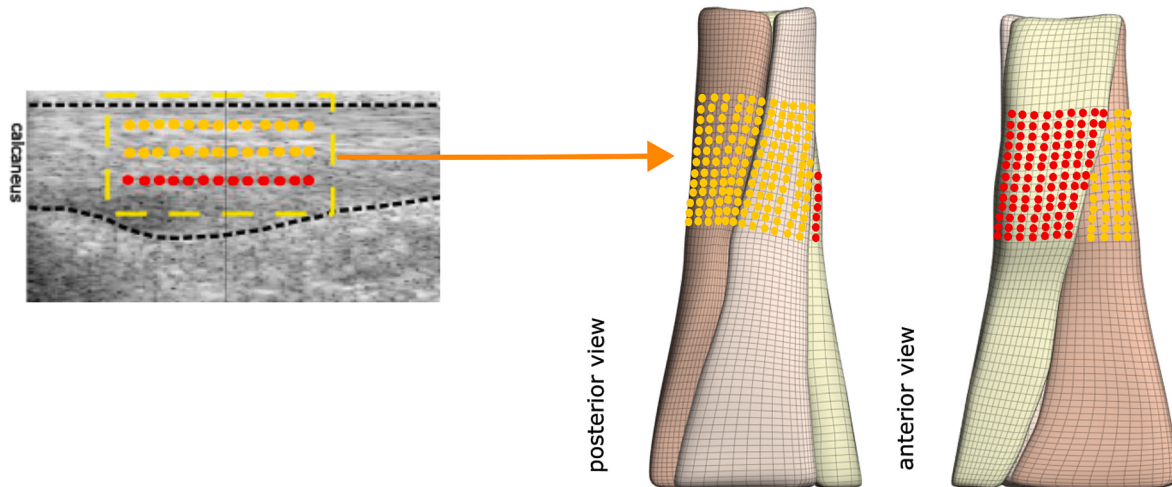


Fig. 3. The figure illustrates the selection of the ROI within the AT FE model, based on experimental data, for the optimization of both material and friction coefficients. In panel A, nodes on the SOL subtendon of the FE model were selected to replicate the overall AT elongation. This elongation was measured as the distance between the calcaneus and the SOL myotendinous junction from the AT reconstruction (observable from the sagittal plane of the 3DfUS image). Nodes located at the very top and bottom of the FE model were excluded to avoid proximity to the boundary conditions and to ensure compliance with Saint-Venant's principle. In panel B, the ROI identified from the ultrasound speckle tracking images was replicated in the FE model. Specific nodes were selected within the FE model: nodes on the SOL subtendon corresponded to the bottom layer of the ROI, while the upper and middle layers were linked to nodes on both the GM and GL subtendons.

was evaluated at each step.

3. Results

3.1. Patient-specific material and friction coefficients

The median patient-specific material coefficients were found to be $C_1 = 5$ MPa (range: 3–11 MPa), $C_4 = 5$ (range: 2–6), and $C_5 = 321$ MPa (range: 201–593 MPa). The average RMS error between SOL_{sim} and MTJ_{exp} was 1.18 ± 0.50 mm and 2.13 ± 0.93 mm for 30% and 60% MVIC, respectively. The average SOL_{sim} was 2.91 ± 0.60 mm and 5.55

± 1.56 mm, for 30% and 60% MVIC, respectively. The median percentage RMS error between SOL_{sim} and MTJ_{exp} was 39.46% (range: 18.01–128.70%) and 32.53% (range: 17.19–60.38%) for 30% and 60% MVIC, respectively. The median patient-specific friction coefficient was found to be 0.962 (range: 0.113–0.999). While most models exhibited an optimal friction coefficient near the upper end of the tested range, four models displayed a local minimum, identified as the optimal solution, located mid-range. This behaviour may be attributed to high non-linearity in the model behaviour. Further details are provided in the *Supplementary Materials*. With the optimized friction coefficients, the average RMS error between the simulated, Δd_{sim} , and the experimental,

Δd_{exp} , differential displacement between SOL and GAS subtendons was 1.35 ± 1.26 mm. The average Δd_{sim} was 2.38 ± 0.48 mm. The median percentage RMS error between the simulated, Δd_{sim} , and the experimental, Δd_{exp} , differential displacement between SOL and GAS subtendons was 59.71% (range: 10.17–366.88%). The final material and friction coefficients and participants details are shown in Table 1.

3.2. Sensitivity analysis

The Sobol indices for the material coefficients are shown in Fig. 4. The elastic modulus of the fibers, C_5 , was the most impactful parameter on the $error_{mp}$, with a first-order sensitivity index S_5 of 0.832. The sensitivity indices S_1 and S_4 were lower, 0.097 and 0.015, respectively, indicating a lesser impact on the $error_{mp}$. When considering interaction effects, ST_1 , ST_4 , and ST_5 were 0.139, 0.058, and 0.890, respectively.

The one-way sensitivity analysis revealed that, on average, $error_{fc}$ changed by $46 \pm 28\%$ across all participants, varying the friction coefficient from 0 to 1 in increments of 0.01. The largest variation in $error_{fc}$ occurred when the friction coefficient ranged between 0 and 0.5 (average change of $38 \pm 26\%$) (Fig. 5A). Beyond a friction coefficient of 0.5, the change in $error_{fc}$ became asymptotic, with a smaller average variation ($22 \pm 25\%$). Δd_{sim} demonstrated an average change of $16 \pm 12\%$ when the friction coefficient was varied from 0 to 1 (Fig. 5B).

4. Discussion

The optimization routine for *in vivo* estimation of material and friction coefficients proved effective in estimating these coefficients for FE models, which simulated the experimental setup. To our knowledge, this is the first study to estimate both patient-specific material coefficients and friction coefficient between two subtendon layers *in vivo* for patients with Achilles tendinopathy.

Our sensitivity analyses revealed that the coefficient C_5 is more influential on the FE model output than the coefficients C_1 and C_4 . This result aligns with the material model described by Weiss et al. (1996) and the experimental setup represented by the FE models. Given that the collagen fibres are straightened during both 30% and 60% MVIC (where strains exceed 2%, surpassing the exponential toe region as described by Wang et al. (2006)), it is reasonable that C_5 would dominate the model's behaviour. Consequently, the contributions of C_4 , which represents the exponential toe region of the collagen fibres, and C_1 , which represents the ground substance matrix embedding the collagen fibres, appear to be less influential on the FE model output.

Previous studies estimated the material properties of the AT in patients with Achilles tendinopathy directly from experimental data. The most commonly used method involves estimating Young's modulus by calculating the slope of the linear region of the stress-strain curve, as employed by Arya and Kulig (2010) and Kulig et al. (2016). Although

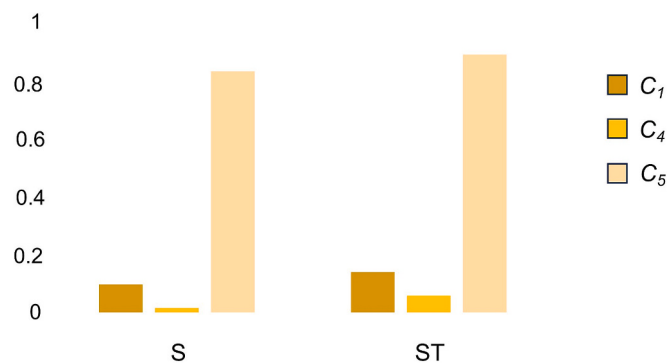


Fig. 4. The first-order (S) and total-order (ST) indices show the high impact of C_5 .

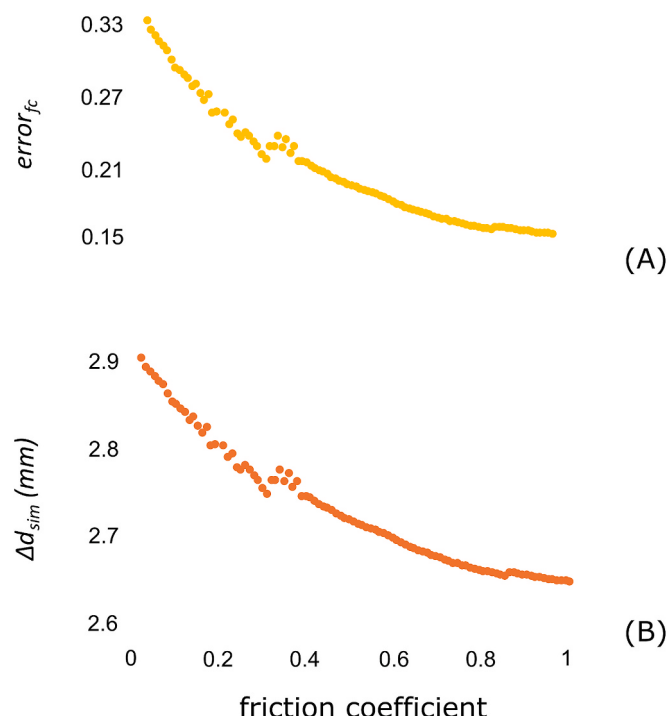


Fig. 5. The change in $error_{fc}$ (A) and Δd_{sim} (B) with varying friction coefficients for Subject 7.

Table 1

Patient characteristics, material and friction coefficients. * indicates model runs influenced by non-linearity affecting optimization.

Subject	Sex	Age (years)	Weight (kg)	Height (m)	VISA-A score	C_1 (MPa)	C_4	C_5 (MPa)	fc
1	F	35	61	1.70	48	8	6	218	0.445*
2	M	26	72	1.91	54	5	4	201	0.757*
3	M	44	73	1.88	79	5	5	258	0.999
4	M	69	71	1.77	93	3	3	124	0.113*
5	M	61	103	1.89	16	4	4	203	0.889
6	F	54	54	1.74	97	3	5	435	0.999
7	M	24	80	1.74	70	5	5	432	0.999
8	M	40	97	1.85	94	4	4	321	0.998
9	M	55	73	1.80	77	4	5	326	0.933
10	M	34	86	1.81	60	11	7	203	0.997
11	M	48	104	1.87	76	4	2	388	0.962
12	M	65	70	1.86	70	5	5	542	0.473*
13	M	50	82	1.72	79	5	5	593	0.986
Median		48	73	1.81	76	5	5	321	0.962

the method used in these studies is straightforward and allows for the direct estimation of Young's modulus from experimental data, it mainly does not account for the complex geometry (Pekala et al., 2017), the unique morphology (Yin et al., 2021) and composite nature of the AT (Weiss, Maker and Govindjee, 1996). Given the influence that both morphological and material characteristics have on AT behaviour (Hansen et al., 2017), it is pivotal to include these characteristics for the estimation of *in vivo* material properties. Therefore, FE models provide a more robust method for estimating material coefficients from experimental data, as they integrate subtendons twisting geometry, patient-specific AT shape, and a constitutive material model that considers both collagen fibres and the ground substance matrix. Due to differences in methodology, it is reasonable to expect that the C_5 coefficient determined in our study may differ from the Young's modulus reported in studies which estimated the Young's modulus from the experimental stress-strain curve (Arya and Kulig, 2010; Kulig et al., 2016). In our study, C_5 was found to be 321 MPa (range: 201–593 MPa), which is lower than the Young's modulus values reported by Arya and Kulig (2010) (818.7 ± 217.0 MPa) and Kulig et al. (2016) (395.3 ± 96.3 MPa). These differences are partially due to methodological differences as well as slightly different populations.

Our study is not the only one to estimate material properties in patients with Achilles tendinopathy using an optimization routine. Shim et al. (2019) also performed material optimization, using 50% MVIC as boundary conditions and minimizing the difference between the FE-predicted shape of the free AT and experimental observations. Results are similar to our study though slightly lower C_5 . This discrepancy could be due to methodological differences, such as not including subtendons. Indeed, the different geometries considered in these studies can significantly influence the FE model output (Handsfield et al., 2017; Hansen et al., 2017). In conclusion, the methodology impacts the outcomes of material properties optimization, along with participant characteristics such as tendinopathy severity and age, which are known to affect AT mechanics (Ekiert, Tomaszewski and Mlyniec, 2021; McMahon and Cook, 2024).

The friction coefficient sensitivity analysis revealed that varying the coefficient from 0 to 1 led to a 16% reduction in differential displacement between subtendons, Δd_{sim} , indicative of the inter-subtendon sliding. Handsfield et al. (2020) explored two different contact conditions which corresponded to a friction coefficient of 0 and 1, respectively, in this study. Similar to our findings, they observed that differential displacement decreased, as the friction coefficient increased. However, Yin et al.'s study (2021) demonstrated that different degrees of twisting, under load, had an influence on the subtendons displacement. The impact of twist alone is also supported by our previous research (Funaro et al., 2022), where we observed changes in differential displacement using three models with varying subtendon twisting geometries. Both studies underscore the complexity of tendon mechanics and suggest that subtendon shape and twist are critical factors influencing differential displacement and subtendon sliding mechanisms. In our study, some of the friction coefficient values appear high, reflecting the optimization's response to specific input parameters, such as muscle forces and geometry. In these cases, due to the geometry of the AT, and the differential force between SOL and GAS muscles, the routine generated high friction values to account for the low differential displacement between subtendons. In contrast, other optimal values were found closer to the mid-range of the evaluated friction coefficient. Further investigation revealed that these four models exhibited high numerical non-linearity in response to changes in the friction coefficient. Although the optimization routine successfully varied the friction coefficient, the underlying models may be affected by high muscle forces, which could limit subtendon contact and contribute to the observed non-linearity. Further studies are needed to clarify these effects, particularly in combination with other factors, such as geometry, and to better understand how these parameters influence model sensitivity to friction coefficient variations and drive friction optimization

outcomes. Given the study's limited sample size, it remains difficult to generalize these findings.

Finally, while MVIC force was patient-specific, a generic triceps surae force distribution was used in the FE model. Since force-sharing can vary between individuals and is altered in Achilles tendinopathy (Crouzier et al., 2018, 2020), this may affect parameter optimization. Despite good alignment with experimental data, future models could benefit from patient-specific force distributions to further improve accuracy and optimization outcomes.

The optimization routine presented in this study enabled the *in vivo* estimation of patient-specific material properties and the friction coefficient between two subtendon layers of the free tendon in patients with Achilles tendinopathy. This study introduces a novel and comprehensive FE modelling routine for the AT, featuring patient-specific geometry, subtendon twisting, material optimization, and friction estimation. Unlike previous work, such as Shim et al. (2019), we uniquely incorporated the twisting structure of all three subtendons. We are also the first to estimate material properties in tendinopathic patients while accounting for this structure. Our optimization used two submaximal *in vivo* contractions, improving robustness compared to prior studies that used only one (Shim et al., 2019). Additionally, by modelling subtendons, we could estimate a patient-specific friction coefficient between two subtendon layers, an improvement over studies using generic values in healthy cohorts (Diniz et al., 2023; Handsfield, 2017; Yin et al., 2021). Although our study is limited to 13 patients and is not yet applicable to clinical practice, it represents the largest sample size available for optimizing FE model parameters in Achilles tendinopathy (Shim et al., 2019).

Some assumptions were necessary to adapt observed tendon behaviour into our model. We assumed homogenous material properties for each subtendon, based on prior work in healthy subjects (Yin et al., 2021), although this may not reflect varying degeneration levels in tendinopathic tendons. Spatially varying properties were not feasible due to data and imaging limitations. Second, we also estimated friction only between the SOL and GAS subtendons, as imaging resolution was insufficient to differentiate GL and GM contributions. Third, we used generic muscle force distributions and a standard subtendon structure, preventing us from capturing individual differences in neural control, muscle volume, or subtendon anatomy. While our routine supports personalized FE modelling in Achilles tendinopathy, further refinement is needed, particularly the integration of patient-specific subtendon geometry and enhanced validation of material and friction parameters. Despite these assumptions and the need for further refinement of the development of these models, the presented method offers a promising tool for gaining deeper insights into the effects of pathological conditions on the AT and has the potential to better inform and guide the recovery process for Achilles tendinopathy in the future.

There are a few limitations in our study. The first is the issue of non-uniqueness within the optimization routine (Nicholson, 2012; Ogden et al., 2004), which is a common problem in inverse FE analysis. We employed two distinct loading conditions to constrain the possible parameter sets that fit the experimental data. Future work will include incorporating an additional condition to refine the solution space. Secondly, identifying individual subtendons *in vivo* using speckle tracking ultrasound remains challenging due to technical limitations and anatomical variability (Pekala et al., 2017; Yin et al., 2021). Displacements may not always correspond precisely to specific subtendons, though it is generally accepted that the SOL subtendon appears at the bottom of the AT image (Clark and Franz, 2018). Our FE model incorporated the most common subtendon twist pattern (Pekala et al., 2017), which, combined with minimal differences between experimental and simulated results, supports the validity of this approach without patient-specific subtendon structure. With recent advances in *in vivo* subtendon geometry estimation (Cone et al., 2023; Lecompte et al., 2025), future models may further benefit from personalized anatomical data. Third, we used hyperelastic materials in line with common practice in FE

models of the AT (Handsfield et al., 2017; Hansen et al., 2017; Shim et al., 2019) and for simulating rehabilitation exercises (Funaro et al., 2025), where viscoelasticity is not essential. However, future clinical applications may require viscoelastic modelling to simulate different loading conditions and to account for loading rate effects. Implementing this would necessitate advanced imaging techniques that were beyond the scope of the present study. Moreover, the material model did not account for the change in material properties due to tendinopathy. Incorporating increased variability within the subtendons from such changes could further affect the simulated strain distribution and, consequently, the estimated parameters. Future studies should therefore consider spatial heterogeneity in material properties, which might be more pronounced in tendinopathic tendons. Finally, cadaver studies could help validate FE models by providing controlled conditions for boundary inputs, subtendon geometry, and detailed deformation data, ultimately enhancing translation to *in vivo* and clinical use.

In conclusion, we developed an optimization routine that enables *in vivo* estimation of patient-specific material coefficients and friction coefficient between two subtendon layers for the free tendon in patients with Achilles tendinopathy. By incorporating a degree of patient-specificity, such as individualized geometry, we were able to capture inter-patient differences in strain patterns. However, limitations remain in fully representing the tendon's complexity, particularly the spatial variability in material properties associated with tendinopathy. Despite these constraints, our approach offers valuable insights into Achilles tendinopathy and holds potential to inform and guide future recovery strategies.

CRediT authorship contribution statement

Alessia Funaro: Writing – review & editing, Writing – original draft, Visualization, Software, Methodology, Investigation, Formal analysis, Data curation, Conceptualization. **Vickie Shim:** Writing – review & editing, Supervision, Methodology, Conceptualization. **Ine Mylle:** Writing – review & editing, Investigation, Data curation. **Chun Vong:** Writing – review & editing, Software, Methodology. **Benedicte Vanwanseele:** Writing – review & editing, Supervision, Methodology, Conceptualization.

Declaration of competing interest

The authors declare that they have no known competing financial interests or personal relationships that could have appeared to influence the work reported in this paper.

Acknowledgements

The authors would like to thank the Research Council KU Leuven for providing financial support for this project (Grant No: C24M/20/053).

Appendix A. Supplementary data

Supplementary data to this article can be found online at <https://doi.org/10.1016/j.biomech.2025.112824>.

References

- Akiba, T., et al., 2019. Optuna: a Next-generation Hyperparameter Optimization Framework. In: *Proceedings of the ACM SIGKDD International Conference on Knowledge Discovery and Data Mining*, pp. 2623–2631. <https://doi.org/10.1145/3292500.3330701>.
- Albracht, K., Arampatzis, A., Baltzopoulos, V., 2008. Assessment of muscle volume and physiological cross-sectional area of the human triceps surae muscle *in vivo*. *J. Biomech.* 41 (10), 2211–2218. <https://doi.org/10.1016/j.biomech.2008.04.020>.
- Arampatzis, A., Karamanidis, K., Albracht, K., 2007. Adaptional responses of the human Achilles tendon by modulation of the applied cyclic strain magnitude. *J. Exp. Biol.* 210 (15), 2743–2753. <https://doi.org/10.1242/jeb.003814>.
- Arnoczky, S.P., Lavagnino, M., Egerbacher, M., 2007. The mechanobiological aetiopathogenesis of tendinopathy: is it the over-stimulation or the under-stimulation of tendon cells? *Int. J. Exp. Pathol.* 88 (4), 217–226. <https://doi.org/10.1111/j.1365-2613.2007.00548.x>.
- Arya, S., Kulig, K., 2010. Tendinopathy alters mechanical and material properties of the Achilles tendon. *J. Appl. Physiol.* 108 (3), 670–675. <https://doi.org/10.1152/japplphysiol.00259.2009>.
- Bogaerts, S., De Brito Carvalho, C., Scheyns, L., Desloovere, K., D'hooge, J., Maes, F., et al., 2017. Evaluation of tissue displacement and regional strain in the Achilles tendon using quantitative high-frequency ultrasound. *PLoS ONE* 12 (7), e0181364. <https://doi.org/10.1371/journal.pone.0181364>.
- Chernak Slane, L., Thelen, D.G., 2014. The use of 2D ultrasound elastography for measuring tendon motion and strain. *J. Biomech.* 47 (3), 750–754. <https://doi.org/10.1016/j.jbiomech.2013.11.023>.
- Clark, W.H., Franz, J.R., 2018. Do triceps surae muscle dynamics govern non-uniform Achilles tendon deformations? *PeerJ* 6, e5182. <https://doi.org/10.7717/peerj.5182>.
- Cone, S.G., et al., 2023. 3D characterization of the triple-bundle Achilles tendon from *in vivo* high-field MRI. *J. Orthop. Res.* 41 (10), 2315–2321. <https://doi.org/10.1002/jor.25654>.
- Couppé, C., et al., 2020. Ultrasound speckle tracking of Achilles tendon in individuals with unilateral tendinopathy: a pilot study. *Eur. J. Appl. Physiol.* 120 (3), 579–589. <https://doi.org/10.1007/s00421-020-04317-5>.
- Craig, C.L., et al., 2003. International physical activity questionnaire: 12-Country reliability and validity. *Med. Sci. Sports Exerc.* 35 (8), 1381–1395. <https://doi.org/10.1249/01.MSS.0000078924.61453.FB>.
- Crouzier, M., et al., 2018. Neuromechanical coupling within the human triceps surae and its consequence on individual force-sharing strategies. *J. Exp. Biol.* 221 (21). <https://doi.org/10.1242/jeb.187260>.
- Crouzier, M., et al., 2020. Force-sharing within the Triceps Surae: an Achilles Heel in Achilles Tendinopathy. *Med. Sci. Sports Exerc.* <https://doi.org/10.1249/MSS.0000000000002229>.
- Crouzier, M., et al., 2022. External rotation of the foot position during plantarflexion increases non-uniform motions of the Achilles tendon. *J. Biomech.* 141 (July). <https://doi.org/10.1016/j.jbiomech.2022.111232>.
- Dandois, F., et al., 2021. Validated ultrasound speckle tracking method for measuring strains of knee collateral ligaments *in-situ* during varus/valgus loading. *Sensors* 21 (5), 1–14. <https://doi.org/10.3390/s21051895>.
- Diniz, P., Quental, C., Violindo, P., et al., 2023. Design and validation of a finite element model of the aponeurotic and free Achilles tendon. *J Orthop Res* 41, 534–545. <https://doi.org/10.1002/jor.25408>.
- Ekierk, M., Tomaszewski, K.A., Mlyniec, A., 2021. The differences in viscoelastic properties of subtendons result from the anatomical tripartite structure of human Achilles tendon - *ex vivo* experimental study and modeling. *Acta Biomater.* 125, 138–153. <https://doi.org/10.1016/j.actbio.2021.02.041>.
- Fedorov, A., et al., 2012. 3D Slicer as an image computing platform for the Quantitative Imaging Network. *Magn. Reson. Imaging* 30 (9), 1323–1341. <https://doi.org/10.1016/j.mri.2012.05.001>.
- Fernandez, J., et al., 2018. Musculoskeletal Modelling and the Physiome Project. In: Pivonka, P. (Ed.), *Multiscale Mechanobiology of Bone Remodeling and Adaptation*. Springer International Publishing, Cham, pp. 123–174. https://doi.org/10.1007/978-3-319-58845-2_3.
- Franz, J.R., et al., 2015. Non-uniform *in vivo* deformations of the human Achilles tendon during walking. *Gait Posture* 41 (1), 192–197. <https://doi.org/10.1016/j.gaitpost.2014.10.001>.
- Funaro, A., et al., 2022. Subject-specific 3D Models to Investigate the Influence of Rehabilitation Exercises and the Twisted Structure on Achilles Tendon Strains. *Front. Bioeng. Biotechnol.* 10 (July), 1–9. <https://doi.org/10.3389/fbio.2022.914137>.
- Funaro, A., et al., 2025. Subject-specific biomechanics influences tendon strains in patients with Achilles tendinopathy. *Sci. Rep.* 15, 1–13. <https://doi.org/10.1038/s41598-024-84202-9>.
- Handsfield, G.G., et al., 2017. A 3D model of the Achilles tendon to determine the mechanisms underlying nonuniform tendon displacements. *J. Biomech.* 51, 17–25. <https://doi.org/10.1016/j.jbiomech.2016.11.062>.
- Handsfield, G.G., et al., 2020. Achilles Subtendon Structure and Behavior as Evidenced from Tendon Imaging and Computational Modeling. *Front. Sports Active Living* 2, 70. <https://doi.org/10.3389/fspor.2020.00070>.
- Hansen, W., et al., 2017. Achilles tendon stress is more sensitive to subject-specific geometry than subject-specific material properties: a finite element analysis. *J. Biomech.* 56, 26–31. <https://doi.org/10.1016/j.jbiomech.2017.02.031>.
- Kulig, K., et al., 2016. Ultrasound-based Tendon Micromorphology Predicts Mechanical Characteristics of Degenerated Tendons. *Ultrasound Med. Biol.* 42 (3), 664–673. <https://doi.org/10.1016/j.ultrasmedbio.2015.11.013>.
- Lecompte, L., et al., 2024. Reduced Intratendinous Sliding in Achilles Tendinopathy during active Plantarflexion Regardless of Horizontal Foot Position. *Scand. J. Med. Sci. Sports* 34 (6), 1–10. <https://doi.org/10.1111/sms.14679>.
- Maas, S.A., et al., 2012. FEBio: Finite elements for Biomechanics. *J. Biomed. Eng.* 134 (1). <https://doi.org/10.1115/1.4005694>.
- Magnusson, S.P., Langberg, H., Kjaer, M., 2010. The pathogenesis of tendinopathy: balancing the response to loading. *Nat. Rev. Rheumatol.* 6 (5), 262–268. <https://doi.org/10.1038/nrheum.2010.43>.
- Lecompte, L., Crouzier, M., Baudry, S., & Vanwanseele, B. (2025) Estimation of the Achilles tendon twist *in vivo* by individual triceps surae muscle stimulation. *Journal of Anatomy*, 246, 86–97. Available from: <https://doi.org/10.1111/joa.14138>.
- McMahon, G., Cook, J., 2024. Female Tendons are from Venus and Male Tendons are from Mars, But Does it Matter for Tendon Health? *Sports medicine (Auckland, N.Z.)*. <https://doi.org/10.1007/s40279-024-02056-7>.

- Merza, E., et al., 2021. Reliability of Human Achilles Tendon Stiffness measures using Freehand 3-D Ultrasound. *Ultrasound Med. Biol.* 47 (4), 973–981. <https://doi.org/10.1016/j.ultrasmedbio.2021.01.002>.
- Nicholson, D.W., 2012. On finite element analysis of an inverse problem in elasticity. *Inverse Prob. Sci. Eng.* 20 (5), 735–748. <https://doi.org/10.1080/17415977.2012.668677>.
- Nuri, L., et al., 2018. Three-dimensional morphology and volume of the free Achilles tendon at rest and under load in people with unilateral mid-portion Achilles tendinopathy. *Exp. Physiol.* 103 (3), 358–369. <https://doi.org/10.1113/EP086673>.
- Shim, V.B., et al., 2014. Subject-specific finite element analysis to characterize the influence of geometry and material properties in Achilles tendon rupture. *J. Biomech.* 47 (15), 3598–3604. <https://doi.org/10.1016/j.jbiomech.2014.10.001>.
- Shim, V.B., et al., 2019. Influence of altered geometry and material properties on tissue stress distribution under load in tendinopathic Achilles tendons – a subject-specific finite element analysis. *J. Biomech.* 82, 142–148. <https://doi.org/10.1016/j.jbiomech.2018.10.027>.
- Sobol, I.M., 2001. Global sensitivity indices for nonlinear mathematical models and their Monte Carlo estimates. *Math. Comput. Simul.* 55 (1–3), 271–280. [https://doi.org/10.1016/S0378-4754\(00\)00270-6](https://doi.org/10.1016/S0378-4754(00)00270-6).
- Thorpe, C.T., Screeen, H.R.C., 2016. Tendon Structure and Composition. In: Ackermann, P.W., Hart, D.A. (Eds.), *Metabolic Influences on Risk for Tendon Disorders*. Springer International Publishing, Cham, pp. 3–10. https://doi.org/10.1007/978-3-319-33943-6_1.
- Virtanen, P., et al., 2020. SciPy 1.0: fundamental algorithms for scientific computing in Python. *Nat. Methods* 17 (3), 261–272. <https://doi.org/10.1038/s41592-019-0686-2>.
- Wang, J.H.C., 2006. Mechanobiology of tendon. *J. Biomech.* 39 (9), 1563–1582. <https://doi.org/10.1016/j.jbiomech.2005.05.011>.
- Wang, T., et al., 2015. Cyclic mechanical stimulation rescues achilles tendon from degeneration in a bioreactor system. *J. Orthop. Res.* 33 (12), 1888–1896. <https://doi.org/10.1002/jor.22960>.
- Weiss, J.A., Maker, B.N., Govindjee, S., 1996. Finite element implementation of incompressible, transversely isotropic hyperelasticity. *Comput. Methods Appl. Mech. Eng.* 135 (1–2), 107–128. [https://doi.org/10.1016/0045-7825\(96\)01035-3](https://doi.org/10.1016/0045-7825(96)01035-3).
- Ogden, R., Saccomandi, G., Sgura, I., 2004. Fitting hyperelastic models to experimental data. *Computational Mechanics* 34, 484–502. <https://doi.org/10.1007/s00466-004-0593-y>.
- Pekala, P.A., Henry, B.M., Ochala, A., et al., 2017. The twisted structure of the Achilles tendon unraveled: A detailed quantitative and qualitative anatomical investigation. *Scand J Med Sci Sports* 27, 1705–1715. <https://doi.org/10.1111/sms.12835>.
- Yin, N.-H., et al. (Eds.), 2021. Individual variation in Achilles tendon morphology and geometry changes susceptibility to injury', *eLife* 10, e63204. <https://doi.org/10.7554/elife.63204>.
- Zimmerman, B.K., Ateshian, G.A., 2018. A Surface-to-Surface Finite Element Algorithm for Large Deformation Frictional Contact in febio. *J. Biomech. Eng.* 140 (8), 1–15. <https://doi.org/10.1115/1.4040497>.